PERGAMON

International Journal of Heat and Mass Transfer 44 (2001) 1161–1170

International Journal of HEAT and MASS TRANSFER

www.elsevier.com/locate/ijhmt

Semi-analytic solutions for freezing induced by evaporative cooling

Carsie A. Hall III [a,*], Calvin Mackie [b]

[a] Department of Mechanical Engineering, University of New Orleans, New Orleans, LA 70148, USA
[b] Department of Mechanical Engineering, Tulane University, New Orleans, LA 70118, USA

Received 21 October 1999; received in revised form 28 April 2000

Abstract

Freezing in a one-dimensional region induced by evaporative cooling is investigated. Semi-analytic solutions in the limit of low mass transfer rates and Stefan numbers are presented. An *n*th order polynomial is used to express the vapor pressure function in terms of the evaporating fluid layer temperature. The freezing of a slab of calcium chloride hexahydrate subject to evaporative cooling of a thin layer of water into air is used to illustrate the utility of the model. Results show the existence of a transition region, depending upon the relative humidity and Biot number, where the fluid layer dry-out time competes with the freeze time of the slab.

1. Introduction

Evaporative cooling has been traditionally used in thermal and nuclear power plants as well as in commercial and industrial HVAC systems where evaporative cooling towers reject cycle waste heat from hot water flowing from condensers. In direct-exchange cooling applications, it is a cost-effective means of delivering comfortable, conditioned air by absorbing sensible heat from hot air through the evaporation of water. Evaporative cooling has also found applications in such areas as the drying of gelcast ceramics [1], shrinkage of foods due to moisture removal [2], cryogenic freezing of ammonia in supersonic flow [3], thermal bending in precision machine tools [4], cooling of high power density electronic devices [5,6], and numerous other passive, low energy consumption processes. It can also be applied to natural gas-assisted air conditioning whereby a phase change material (PCM) is successively charged by pulsed natural gas heating and subsequently discharged to continuously provide evaporative cooling of hot outside air. In any process, however, evaporative cooling would have an economic advantage over forced flow cooling since additional capital equipment (i.e., pumps and valves) and associated energy expenditure would have to be considered.

The literature on evaporative cooling, including fundamentals and applications, is vast and will not be reviewed here. Some notable studies on evaporative film and spray cooling, including appropriate references to the literature therein, include Yan and Lin [7] and Kachhwaha et al. [8]. However, the application of evaporative cooling to solidification processes is scarce at best. On the other hand, solidification (and melting) of materials due to isothermal, uniform heat flux, convective, and radiative boundary conditions are more common. In fact, a number of investigations have appeared in the literature on the freezing of slabs, subject to various types of boundary conditions. Alexiades and Solomon [9] provided an excellent compilation of various types of melting and freezing studies, with a number of analytic solutions to one-phase and two-phase one-dimensional Stefan-type problems with different types of boundary conditions (i.e., insulated, isothermal, uniform flux, and convective). Goodling and Khader [10] used an implicit finite difference method to solve the problem of inward solidification of one-dimensional slabs, cylinders, and spheres subject to convective and radiative cooling at their outer surfaces. An investigation on phase

* Corresponding author. Tel.: +1-504-280-6167; fax: +1-504-280-5539.
E-mail address: cahall@uno.edu (C.A. Hall III).

0017-9310/01/$ - see front matter
PII: S0017-9310(00)00154-X

Nomenclature

Bi	Biot number
c	specific heat
D	thickness of one-dimensional region
D_{12}	binary diffusion coefficient
g^*	low-rate mass transfer coefficient
h^*	convective heat transfer coefficient at zero net mass transfer
$\bar{h}$	average heat transfer coefficient over liquid layer
h_{fg}	latent heat of vaporization
h_{sf}	latent heat of fusion
Ja	modified Jakob number
k	thermal conductivity
Le	Lewis number
m	vapor mass fraction
M	molecular weight or molar mass
$\dot{m}''$	fluid layer evaporation flux
$\dot{m}''*$	dimensionless fluid layer evaporation flux
P	pressure
Ste	Stefan number
t	time
T	temperature
X	vapor mole fraction
y	coordinate location
Y	dimensionless coordinate location

Greek symbols

α	thermal diffusivity
δ	solid region thickness
Δ	dimensionless solid region thickness
ϕ	relative humidity
λ	fluid layer thickness
Λ	dimensionless fluid layer thickness
θ	dimensionless temperature
ρ	density
τ	dimensionless time or Fourier number

Subscripts

atm	parameter evaluated at atmospheric conditions
f	liquid or fluid
g	gas
m	parameter evaluated at solid–liquid interface conditions
0	initial value
s	solid region
sat	parameter evaluated at saturation conditions
∞	parameter evaluated at far field conditions

change caused by aerodynamic and radiative cooling (or heating) was performed by Chung and Yeh [11] for a one-dimensional slab using Biot's variational method and Goodman's integral method. Both methods required subsequent numerical integration. The perturbation expansion method was used by Yan and Huang [12] to obtain solutions for one-dimensional solidification (or melting) of a slab subject to convective and radiative cooling (or heating) on one side and an adiabatic condition on the other. Seeniraj and Bose [13] provided asymptotic solutions for one-dimensional solidification (and melting) of slabs, cylinders, and spheres subject to aerodynamic and radiative cooling (or heating). Prud'homme et al. [14] applied the method of strained coordinates to the inward solidification of slabs, cylinders, and spheres. With the liquid initially at its fusion temperature, freezing was induced by: isothermal cooling, uniform heat flux cooling, or convective cooling. Recently, Hall et al. [15] provided unified semi-analytic solutions for the solidification of slabs, cylinders, and spheres (with two coalescing freeze fronts) subject to convective and radiative boundary conditions. Therefore, to the best of the present authors' knowledge, it appears that no solutions have been presented in the literature on the freezing of one-dimensional slabs due to surface evaporative cooling.

In the present paper, a one-dimensional model of a solidifying slab subject to evaporative cooling by a thin liquid layer is presented. With various fixed dimensionless parameters such as the slab-thickness-to-initial-fluid-layer thickness ratio, Stefan number, modified Jakob number, Lewis number, fluid-layer-to-ambient-gas molar mass ratio, and material solid-to-fluid-layer volumetric heat capacity ratio, the effects of parameters such as relative humidity and Biot number on the dry-out characteristics of the fluid layer and the freeze characteristics of the slab are determined. An example is given to illustrate the applicability of the model.

2. Problem formulation

Consider the physical model shown in Fig. 1 of a one-dimensional region of thickness D undergoing solidification. With the material undergoing solidification ini-

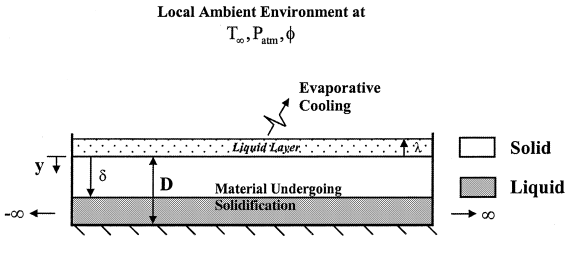

Fig. 1. One-dimensional model for freezing due to an evaporating fluid layer.

tially at its fusion temperature, T_m, a thin, stagnant liquid layer of initial thickness, λ_0 ($\ll D$), and temperature, T_m, suddenly comes into direct contact with the molten material, inducing solidification at the material–liquid layer interface due to evaporative cooling. The bottom surface of the material is maintained under adiabatic conditions. Furthermore, it is assumed that the solid–liquid interface remains planar and sharp, and the remaining molten layer within the material is maintained at a uniform temperature of T_m. Therefore, only the solid region is analyzed, and motion due to density change upon phase change is not significant (i.e., $\rho_l = \rho_s$; no solidification shrinkage). Furthermore, the liquid layer is exposed to a local ambient gaseous environment (herein considered a binary mixture), which is maintained at a temperature of T_∞, atmospheric pressure, P_{atm}, and relative humidity, ϕ. All thermophysical properties are assumed constant.

The transient one-dimensional temperature distribution in the material's solidifying region is described by the heat diffusion equation,

$$\frac{\partial T_s}{\partial t} = \alpha_s \frac{\partial^2 T_s}{\partial y^2} \tag{1}$$

subject to the initial condition,

$$T_s(y, t=0) = T_f(t=0) = T_m, \tag{2}$$

where α_s is the thermal diffusivity of the solid and T_f is the lumped fluid (liquid) layer temperature. The corresponding boundary conditions are given by

$$k_s \left.\frac{\partial T_s}{\partial y}\right|_{y=0} = \dot{m}'' h_{fg} + \bar{h}(T_f - T_\infty), \tag{3}$$

$$T_s(y=\delta) = T_m \tag{4}$$

and the Stefan condition is expressed as

$$k_s \left.\frac{\partial T_s}{\partial y}\right|_{y=\delta} = \rho_s h_{sf} \frac{d\delta}{dt}. \tag{5}$$

Eq. (3) is obtained by performing an energy balance on a differential element of fluid in the liquid layer, which is considered lumped with negligible thermal inertia (e.g., $(\rho_f c_f \lambda) dT_f/dt$ is small since the initial fluid layer thickness λ_0 is negligibly small); $\dot{m}''$ is the evaporation flux (or total mass flow rate per unit area) of the liquid, h_{fg} is the latent heat of vaporization of the liquid, and $\bar{h}$ is the average convective heat transfer coefficient over the liquid layer. In Eq. (5), h_{sf} is the latent heat of fusion of the material and δ is the instantaneous location of the solid–liquid interface within the material.

In order to account for the evaporating fluid layer, the conservation of fluid layer mass requires that

$$\dot{m}'' = -\rho_f \frac{d\lambda}{dt}, \tag{6}$$

subject to the initial condition,

$$\lambda(t=0) = \lambda_0. \tag{7}$$

Upon introducing the following non-dimensional parameters:

$$Y = \frac{y}{D}, \quad \tau = \frac{t}{D^2/\alpha_s}, \quad \theta = \frac{T - T_\infty}{T_m - T_\infty},$$
$$\Delta = \frac{\delta}{D}, \quad \Lambda = \frac{\lambda}{\lambda_0}, \quad \dot{m}''^* = \frac{\lambda_0 \dot{m}''}{\rho_f \alpha_f}, \tag{8}$$

the resulting equation in the solidified layer transforms as

$$\frac{\partial \theta_s}{\partial \tau} = \frac{\partial^2 \theta_s}{\partial Y^2}, \tag{9}$$

and the initial and boundary conditions transform, accordingly, as

$$\theta_s(Y, \tau=0) = \theta_f(\tau=0) = 1, \tag{10}$$

$$\left.\frac{\partial \theta_s}{\partial Y}\right|_{Y=0} = \frac{BiLe^{2/3}}{Ja}(m_f - m_\infty) + Bi\theta_f, \tag{11}$$

$$\theta_s(Y=\Delta) = 1, \tag{12}$$

while the Stefan condition transforms to

$$\left.\frac{\partial \theta_s}{\partial Y}\right|_{Y=\Delta} = \frac{1}{Ste}\frac{d\Delta}{d\tau}, \tag{13}$$

where the Biot (Bi), Lewis (Le), modified Jakob (Ja), and Stefan (Ste) numbers are, respectively, defined as

$$Bi = \frac{\bar{h}D}{k_s}, \quad Le = \frac{D_{12}}{\alpha_f} = \frac{Pr}{Sc},$$
$$Ja = \frac{c_f(T_m - T_\infty)}{h_{fg}}, \quad Ste = \frac{c_s(T_m - T_\infty)}{h_{sf}}, \tag{14}$$

in which Pr ($=\nu_f/\alpha_f$) is the Prandtl number and Sc ($=\nu_f/D_{12}$) is the Schmidt number. The non-dimensional conservation of mass for the evaporating fluid layer is written as

$$-\frac{d\Delta}{d\tau} = \left(\frac{D}{\lambda_0}\right)\left[\frac{(\rho c)_s}{(\rho c)_f}\right] BiLe^{-2/3}(m_f - m_\infty), \tag{15}$$

with $\Lambda(\tau=0) = 1$. It is noted that in Eqs. (14) and (15), D_{12} is the binary diffusion coefficient and m_f and m_∞ are, respectively, the mass fractions of vapor near the liquid–gas interface and far away in the free stream. In Eq. (11), the evaporation flux at low mass transfer rates, described by a reduced form of an expression found in [16], is given by

$$\dot{m}'' = g^*(m_f - m_\infty). \tag{16}$$

In Eq. (16), g^* is the low-rate mass transfer coefficient, given by the heat and mass transfer analogy [16], i.e.,

$$g^* = \frac{h^*}{c_f} Le^{2/3} \tag{17}$$

in which h^* is the convective heat transfer coefficient at zero net mass transfer, which is approximated as the average convective heat transfer coefficient $\bar{h}$. Furthermore, the vapor mass fraction difference $(m_f - m_\infty)$ is known as the low-rate mass transfer driving factor, which results when the vapor mass fraction at the liquid–gas interface is much less than unity. These vapor mass fractions can be calculated by

$$\begin{aligned} m_f &= \frac{X_f M_f}{X_f M_f + (1 - X_f) M_g} \\ &= \frac{P_{sat}(T_f)}{P_{sat}(T_f) + [P_{atm} - P_{sat}(T_f)] M_g / M_f} \cong \frac{M_f}{M_g} \frac{P_{sat}(T_f)}{P_{atm}} \end{aligned} \tag{18}$$

and

$$\begin{aligned} m_\infty &= \frac{X_\infty M_f}{X_\infty M_f + (1 - X_\infty) M_g} \\ &= \frac{\phi P_{sat}(T_\infty)}{\phi P_{sat}(T_\infty) + [P_{atm} - \phi P_{sat}(T_\infty)] M_g / M_f}, \end{aligned} \tag{19}$$

where M_f and M_g are the molecular weights (or molar masses) of the liquid and gas, respectively, and X_f and X_∞ are, respectively, the mole fractions of vapor at the liquid–gas interface and far away in the free stream. These mole fractions are calculated by [17]

$$X_f = \frac{P_{sat}(T_f)}{P_{atm}} \tag{20}$$

and

$$X_\infty = \frac{\phi P_{sat}(T_\infty)}{P_{atm}}, \tag{21}$$

where $P_{sat}(T_f)$ is the saturation pressure of the vapor at the local liquid temperature and $P_{sat}(T_\infty)$ is the saturation pressure of the vapor at the local ambient temperature. The approximate equality in Eq. (18) results from the assumption that the vapor mole fraction at the liquid–gas interface is much smaller than unity and the molecular weights of the liquid and gas are of the same order of magnitude.

Although saturation property data for various fluids given in the literature appears in tabular form, a polynomial curve-fit allows a convenient algebraic representation of these data. In the context of the present model, analytic or semi-analytic solutions are possible in the limit of low Stefan numbers.

3. Semi-analytic solution

In order to obtain a semi-analytic solution to the present problem as formulated, phase change is assumed to progress in a quasi-steady manner, which is consistent with the low Stefan number limit. Therefore, the solution to the quasi-steady form of Eq. (9) is given by

$$\theta_s(Y, \tau) = [1 - \theta_f(\tau)] \frac{Y}{\Delta(\tau)} + \theta_f(\tau), \tag{22}$$

which implies that Eqs. (11) and (13), respectively, become

$$\frac{BiLe^{2/3}}{Ja} (m_f - m_\infty) + Bi\theta_f = \frac{1 - \theta_f}{\Delta}, \tag{23}$$

$$\frac{1}{Ste} \left(\frac{\Delta - \Delta_0}{\Delta \tau} \right) = \frac{1 - \theta_f}{\Delta}, \tag{24}$$

where a forward difference approximation has been made on the freeze rate term in Eq. (13). Upon substituting Eqs. (18) and (19) into Eq. (23) and rearranging terms, the following equation results:

$$\frac{BiLe^{2/3}}{Ja} \left\{ F(\theta_f) - G\left[P^*_{sat}(0), \phi \right] \right\} + \left(Bi + \frac{1}{\Delta} \right) \theta_f - \frac{1}{\Delta} = 0, \tag{25}$$

where

$$F(\theta_f) = \frac{M_f}{M_g} P^*_{sat}(\theta_f) \tag{26}$$

and the a priori known function G is expressed as

$$G\left[P^*_{sat}(0), \phi \right] = \frac{\phi P^*_{sat}(0)}{\phi P^*_{sat}(0) + \left[1 - \phi P^*_{sat}(0) \right] M_g / M_f}, \tag{27}$$

where $P^*_{sat}(0)$ is the dimensionless saturation pressure function evaluated at ambient conditions. Furthermore, if the function $P^*_{sat}(\theta_f)$ in Eq. (26) is assumed to be a polynomial of degree n, then the final form of Eq. (25) is expressed as

$$\begin{aligned} &\frac{BiLe^{2/3}}{Ja} \left\{ \frac{M_f}{M_g} \left[a_n \theta_f^n + a_{n-1} \theta_f^{n-1} + \cdots + a_0 \right] \right. \\ &\left. - G\left[P^*_{sat}(0), \phi \right] \right\} + \left(Bi + \frac{1}{\Delta} \right) \theta_f - \frac{1}{\Delta} = 0, \end{aligned} \tag{28}$$

which can be solved analytically or numerically once the order of the polynomial (with associated coefficients $a_n, a_{n-1}, \ldots, a_0$) is specified. Moreover, Eq. (15) can be discretized and cast in the following form:

$$\Lambda^n = \Lambda^{n-1} - \left(\frac{D}{\lambda_0} \right) \left[\frac{(\rho c)_s}{(\rho c)_f} \right] BiLe^{-2/3} (m_f - m_\infty) \Delta \tau. \tag{29}$$

Within the framework of the present formulation, an expression for the dependent variables Δ, Λ, and θ_f can be written functionally as

$$\begin{aligned} (\Delta, \Lambda, \theta_f) = f \left[Bi, Ja, Le, Ste, \frac{M_f}{M_g}, P^*_{sat}(0), \phi, a_n, a_{n-1}, \ldots a_0, \right. \\ \left. \frac{D}{\lambda_0}, \frac{(\rho c)_s}{(\rho c)_f}, \tau \right]. \end{aligned} \tag{30}$$

4. Solution procedure

The solid–liquid interface is advanced a small increment from Δ_{n-1} to Δ_n; Eq. (28) is then solved for the fluid layer temperature, $\theta_f{}^n$. The elapsed time, $\Delta\tau_n$, in advancing the interface from Δ_{n-1} to Δ_n, corresponding to $\theta_f{}^n$, is determined by solving Eq. (24). The current time associated with the previous step is calculated using $\tau_n = \tau_{n-1} + \Delta\tau_n$. Eq. (29) is then solved to find the evaporating fluid layer thickness, Λ^n. This procedure is repeated until Λ^n reaches zero or until Δ_n reaches unity.

5. Results and discussion

In what follows, the solution procedure outlined in the previous section is illustrated by a practical example. Consider the freezing of a slab of Calcium Chloride Hexahydrate ($CaCl_2 \cdot 6H_2O$), induced by an evaporating layer of water into air. The relevant thermophysical properties of $CaCl_2 \cdot 6H_2O$ and water are shown in Table 1. With the molten slab initially at its fusion temperature (27°C), and with a thin, stagnant layer of water, also initially at 27°C, that suddenly comes into contact with the slab, freezing occurs by evaporating the water into air. The ambient air is maintained at a temperature of 25°C and a pressure of 1 atm. A second-order polynomial curve-fit of the vapor pressure data for water in the range of $10°C \leqslant T_{sat} \leqslant 40°C$ is used in obtaining the present semi-analytic solutions [4]. This second-order polynomial is given by $P_{sat}(T_{sat}) = 5T_{sat}^2 - 50.8T_{sat} + 1282.1$, where P_{sat} is expressed in pascals (Pa) and T_{sat} is expressed in degrees Celsius (°C). This curve-fit results in an error of approximately 1% at 25°C and about 0.3% at 30°C as compared to the vapor pressure data compiled in [18]. The corresponding fixed dimensionless parameters are also shown in Table 1. It should be pointed out here that the effects of supercooling and phase segregation of the $CaCl_2 \cdot 6H_2O$ slab are neglected [9]. Furthermore, the normally dendritic growth of the $CaCl_2 \cdot 6H_2O$ freeze front is neglected and the solid–liquid interface is regarded as sharp since the interface region is typically very thin [9].

Now consider Eq. (26), where $P^*_{sat}(\theta_f)$ is a second-order polynomial used in Eq. (28). The generalized solution for the dimensionless fluid layer temperature as a function of material properties and environmental conditions, in the form of various dimensionless parameters, can be written as

$$\theta_f = \left\{ \left\langle \left(\frac{a_2}{2Ja}\frac{M_f}{M_g} \right)^{-1} \left[\frac{a_1}{Ja}\frac{M_f}{M_g} + Le^{-2/3}\left[1 + (Bi\Delta)^{-1} \right] \right] \right\rangle^2 - \left(\frac{a_2}{Ja}\frac{M_f}{M_g} \right)^{-1} \left[\frac{a_0}{Ja}\frac{M_f}{M_g} - \frac{G\left[P^*_{sat}(0), \phi\right]}{Ja} - Le^{-2/3}(Bi\Delta)^{-1} \right] \right\}^{1/2} - \left(\frac{a_2}{2Ja}\frac{M_f}{M_g} \right)^{-1} \left[\frac{a_1}{Ja}\frac{M_f}{M_g} + Le^{-2/3}\left[1 + (Bi\Delta)^{-1} \right] \right], \tag{31}$$

where the non-dimensional coefficients a_2, a_1, and a_0 are given, respectively, by

$$a_2 = \frac{a'_2(T_m - T_\infty)^2}{P_{atm}}, \quad a_1 = \frac{\left(2a'_2T_\infty + a'_1\right)(T_m - T_\infty)}{P_{atm}}, \quad \text{and } a_0 = \frac{a'_0 + T_\infty\left(a'_2T_\infty + a'_1\right)}{P_{atm}} \tag{32}$$

in which a'_2, a'_1, and a'_0 are the actual coefficients resulting from a second-order polynomial curve-fit of the vapor pressure data. Within the context of the present example,

Table 1
Thermophysical properties of calcium chloride hexahydrate [9] and water [18] that are used in the present study

Property	$CaCl_2 \cdot 6H_2O$	Water
ρ (kg/m^3)	1700 (solid)	997[a]
c (J/kg °C)	2210 (solid)	4188[a]
k (W/m °C)	1.08 (solid)	–
h_{sf} (J/kg)	190,000	–
T_m (°C)	27	–
h_{fg} (J/kg)	–	2,437,560[b]
Corresponding dimensionless parameters		
$Le = 1$	$a_0 = 3.096 \times 10^{-2}$	
$Ja = 3.436 \times 10^{-3}$	$a_1 = 3.932 \times 10^{-3}$	
$Ste = 2.319 \times 10^{-2}$	$a_2 = 1.974 \times 10^{-4}$	
$(\rho c)_s/(\rho c)_f = 0.9$		
$P^*_{sat}(0) = 3.127 \times 10^{-2}$		
$M_g/M_f = 1.6$[c]		

[a] Evaluated at 25°C.
[b] Evaluated at 27°C by interpolation.
[c] Evaluated using $M_g = M_{air} = 28.97$ and $M_f = M_{water} = 18.02$.

these coefficients are, respectively, 5, −50.8, and 1282.1 as indicated in the aforementioned curve-fit of the vapor pressure data for water. These numbers are reflected in the coefficients a_2, a_1, and a_0 shown in equation set (32), with numerical values listed in Table 1.

5.1. A comparative exercise: the isothermal limit

Consider the solution for the dimensionless fluid layer temperature shown in Eq. (31). In the limit of very large Biot numbers ($Bi \to \infty$), and as $a_0 M_f/M_g \to G$, it can be shown that the dimensionless fluid layer temperature approaches zero. As a result, freezing of the slab is due to that of surface isothermal cooling. In the present example, a close approximation to isothermal freezing is achieved as the relative humidity approaches 100% ($\phi \to 1$), i.e.,

$$\frac{a_0}{M_g/M_f} = 1.935 \times 10^{-2} \quad \text{and} \quad G(\phi = 1) = 1.977 \times 10^{-2}.$$

It is observed that these calculations differ by approximately 2%, and as the relative humidity decreases towards zero, the approximation becomes less valid. In fact, in the isothermal limit, the solutions are independent of the relative humidity near saturation conditions since the vapor pressure of the water near the liquid-gas interface would approach the vapor pressure of the water in the free stream. As a result, the mass fraction of water vapor near the liquid–gas interface approaches that of the free stream and the potential for mass transfer collapses to zero.

Shown in Fig. 2 is the temporal progression of the $CaCl_2 \cdot 6H_2O$ solid–liquid interface in the approximation to the isothermal limit. Closed-form, quasi-steady solutions for the solid–liquid interface position and surface temperature for isothermal freezing of a slab are superimposed on the figure. These solutions are written in non-dimensional form from the quasi-steady solutions found in Alexiades and Solomon [9] in the limit as $Bi \to \infty$, i.e.,

$$\Delta' = \sqrt{\frac{1}{Bi^2} + 2 \cdot Ste \cdot \tau} - \frac{1}{Bi} \to \sqrt{2 \cdot Ste \cdot \tau}, \tag{33}$$

$$\theta_f' = \frac{1}{1 + Bi\Delta'} \to 0. \tag{34}$$

Eq. (33) converges to the exact Neumann solution as $Bi \to \infty$ and when the parameter in the transcendental equation of Neumann's solution is approximated by $(Ste/2)^{1/2}$, which is valid in the limit low Stefan numbers [9]. These solutions can also be derived from Eqs. (11) and (13) by setting $m_f = m_\infty$ and subsequently integrating.

In Fig. 2, excellent agreement can be observed in the temporal progression of the freeze front location in the isothermal limit, which is simulated by setting $Bi = 10^{30}$ and $\phi = 1$. The differences can be attributed to the aforementioned 2% difference in $a_0 M_f/M_g$ and G, which results in a dimensionless fluid layer temperature of approximately 0.072. This effectively slows down the motion of the interface as shown in the figure.

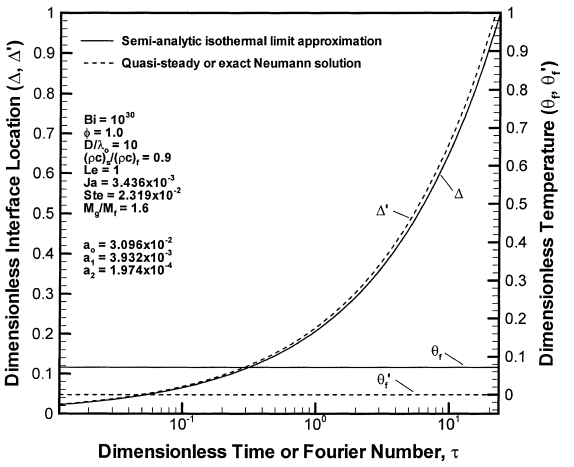

Fig. 2. Temporal development of dimensionless solid–liquid interface position, dimensionless solid–liquid interface position without fluid layer, dimensionless fluid layer temperature, and dimensionless solidified region surface temperature (without fluid layer) in the approximate isothermal limit.

5.2. Effect of relative humidity and finite Biot number

In analyzing the simultaneous progression of the $CaCl_2 \cdot H_2O$ freeze front and fluid layer liquid–gas interface, the dimensionless parameters contained in Table 1 remain fixed. The other dimensionless parameter that remains fixed throughout this section is the slab thickness-to-initial-fluid-layer thickness ratio, which is kept at $D/\lambda_0 = 10$. This value is chosen to represent a lower bound on the allowable thickness ratio in order to ensure the validity of the lumped capacity analysis of the fluid layer. Therefore, for values lower than 10, the analysis would have to include the finite thermal resistance of and, hence, thermal gradients within the fluid layer.

The temporal development of the dimensionless solid–liquid interface position, fluid layer liquid–gas interface position, and dimensionless fluid layer temperature are all shown in Fig. 3. The results shown in this figure pertain to the evaporation of water into dry air, where the relative humidity is zero ($\phi = 0$). The Biot number is held at unity ($Bi = 1$). Superimposed on this figure is the dimensionless freeze front location and dimensionless slab surface temperature without evaporative cooling. The first interpretation that can be made is that when all the other parameters are fixed, including

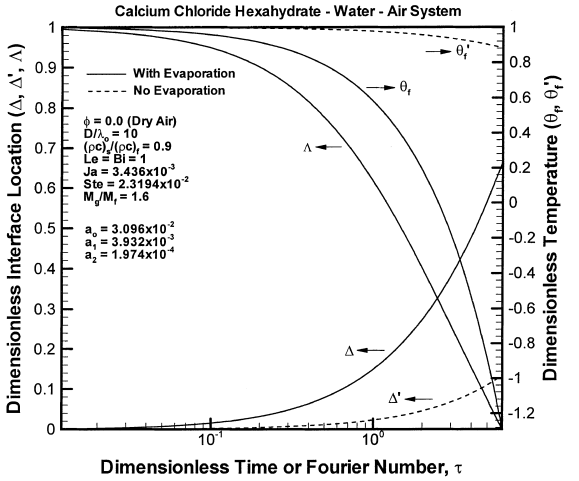

Fig. 3. Temporal development of dimensionless solid–liquid interface position (with and without evaporative cooling), dimensionless fluid layer liquid–gas interface position, dimensionless fluid layer temperature, and dimensionless solidified region surface temperature (without evaporative cooling) at 0% relative humidity (dry air).

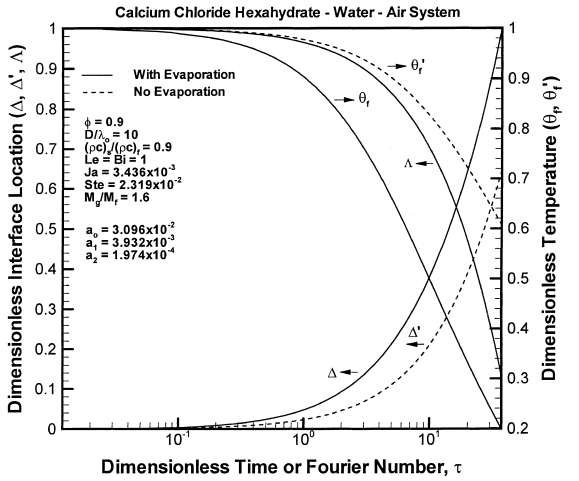

Fig. 4. Temporal development of dimensionless solid–liquid interface position (with and without evaporative cooling), dimensionless fluid layer liquid–gas interface position, dimensionless fluid layer temperature, and dimensionless solidified region surface temperature (without evaporative cooling) at 90% relative humidity.

the Biot number, the case of evaporating water into dry air results in minimum dry-out time and incomplete solidification of the slab. The dry-out time is defined as the time necessary for complete evaporation of the fluid layer. In Fig. 3, the dry-out time occurs at approximately $\tau_{dry} = 6.165$, and about 66.8% of the slab thickness is solidified at dry-out. Without evaporative cooling, the fraction of solidified slab thickness is only about 13.4% at the same time corresponding to dry-out. Also, the effect of maximum evaporative cooling ($\phi = 0$) reduces the dimensionless fluid layer temperature from approximately $\theta_f' = 0.8818$ (without evaporative cooling) to about $\theta_f = -1.292$, which indicates cooling below the ambient air temperature.

Fig. 4 illustrates the effect of increasing the relative humidity to 90%, with all of the same conditions as in Fig. 3. The first observation is that dry-out does not occur, as the time for complete solidification of the slab occurs at approximately $\tau_f = 36.9$. In fact, about 13.21% of the fluid layer remains upon complete solidification. This is due simply to the fact that the much higher relative humidity slows down significantly the evaporation process as compared to the solidification process. In the absence of evaporation, only about 64.67% of the slab is solidified at the time corresponding to complete solidification of the slab with evaporative cooling. Furthermore, evaporative cooling reduces the fluid layer temperature from approximately $\theta_f' = 0.6073$ (without evaporative cooling) to about $\theta_f = 0.1993$.

The effect of relative humidity, ranging from 50% to 90%, on the temporal progression of the ratio of solidified thickness with evaporative cooling to solidified thickness without evaporative cooling is shown in Fig. 5, with the Biot number fixed at unity. In the figure, a solid thickness ratio decrease, ranging from approximately 4.49 at 50% relative humidity down to about 2.18 at 90% relative humidity, can be observed at early times. The characteristic decrease in thickness ratio as time progresses (for all representative relative humidities) can be

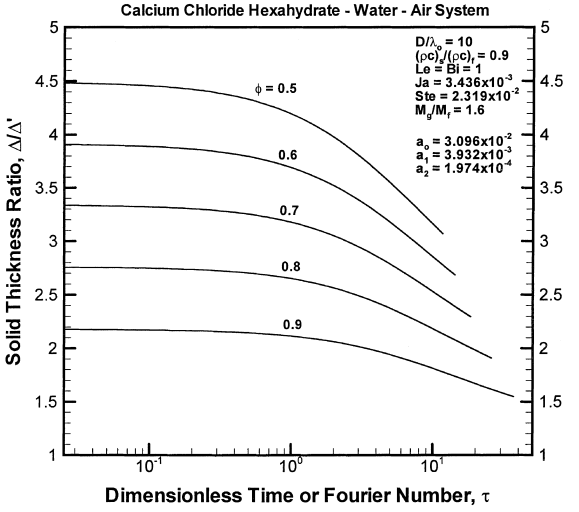

Fig. 5. Effect of relative humidity on the ratio of solidified thickness with evaporative cooling to solidified thickness without evaporative cooling.

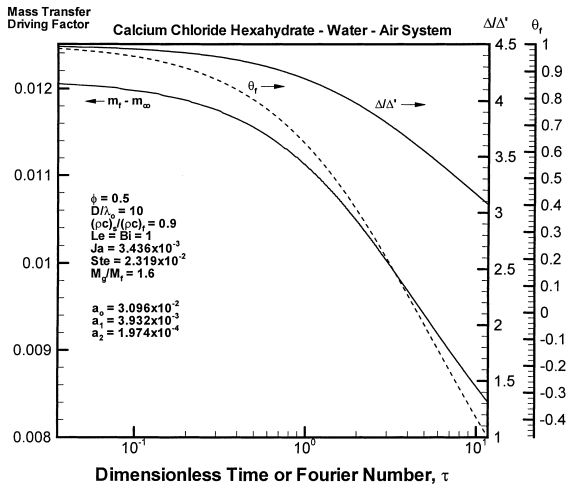

Fig. 6. Temporal development of mass transfer driving factor with solidified thickness ratio and dimensionless fluid layer temperature superimposed.

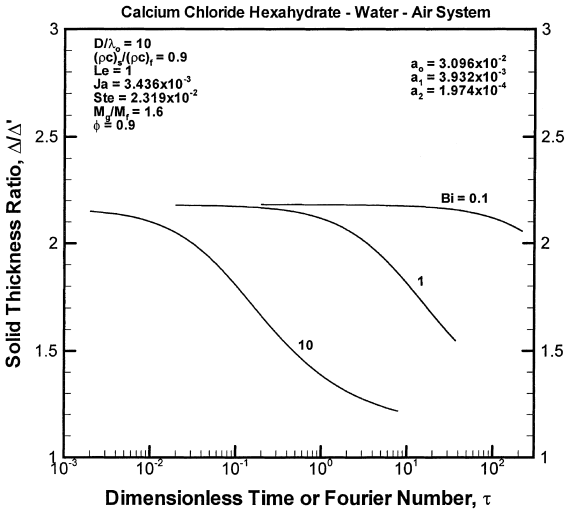

Fig. 7. Effect of Biot number on the ratio of solidified thickness with evaporative cooling to solidified thickness without evaporative cooling.

explained in Fig. 6, with a fixed relative humidity of 50%. The temporal decrease in thickness ratio corresponds to a temporal decrease in mass transfer driving factor $(m_f - m_\infty)$, which is simply due to the fact that as the fluid layer temperature decreases, the vapor pressure at the fluid layer liquid–gas interface decreases. In fact, the mass transfer driving factor drops from about 0.01209 initially to approximately 0.0084 just before dry-out. At dry-out time or freeze time (Fig. 5), the thickness ratio drops from around 3.07 to about 1.55 as the relative humidity increases from 50 to 90%. In addition, the dry-out times for relative humidities of 50%, 60%, 70%, and 80% are 11.7, 14.3, 18.4, and 25.9, respectively. It should be recalled from Fig. 4 that at 90% relative humidity, complete solidification is achieved. Therefore, the transition from dry-out to complete solidification occurs between 80% and 90% relative humidity.

In Fig. 7, the effect of Biot number on the temporal development of the thickness ratio is illustrated for a fixed relative humidity of 90%. At early times (as $\tau \to 0$), it can be observed that the thickness ratio approaches an asymptotic value of 2.18 for all representative Biot numbers. Upon dry-out or complete solidification, the thickness ratio decreases from 2.06 to 1.55 to 1.22 at Biot numbers of 0.1, 1, and 10, respectively. For Biot numbers of 0.1 and 1, the freeze times are, respectively, $\tau_f = 215$ and $\tau_f = 36.9$ while at a Biot number of 10, the dry-out time is approximately $\tau_{dry} = 7.9$. Therefore, when the relative humidity is fixed at 90%, the transition between dry-out and complete solidification occurs between Biot numbers of 1 and 10. An excellent illustration of the transition between dry-out and complete solidification is shown in Fig. 8, which shows the effect of relative humidity on the dry-out or freeze time at Biot

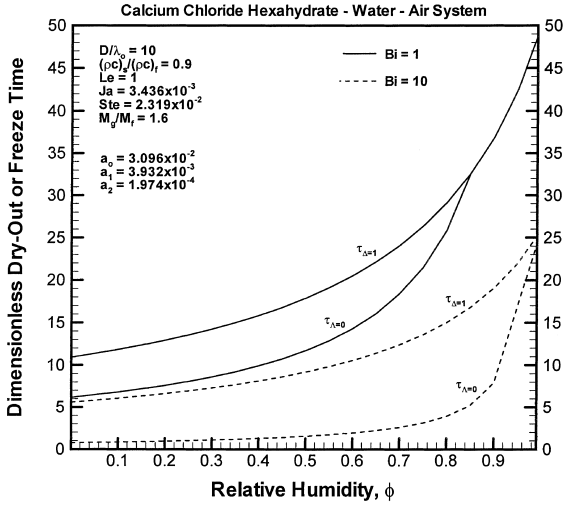

Fig. 8. Comparison of fluid layer evaporation time (dry-out) and material freeze time as a function of relative humidity for selected Biot numbers.

numbers of 1 and 10. It should be noted that the curve labeled "$\tau_{\Lambda=0}$" corresponds to the dry-out time and the curve labeled "$\tau_{\Lambda=1}$" corresponds to the freeze time when a non-zero fluid layer thickness is artificially maintained, which allows complete solidification of the slab. For example, at a relative humidity of 0% (dry air), if a finite fluid layer thickness is artificially maintained, then the freeze time would occur at $\tau_f = 10.9$ instead of drying out at $\tau_{dry} = 6.165$. In the figure, it can be observed that at $Bi = 1$, the transition between dry-out and

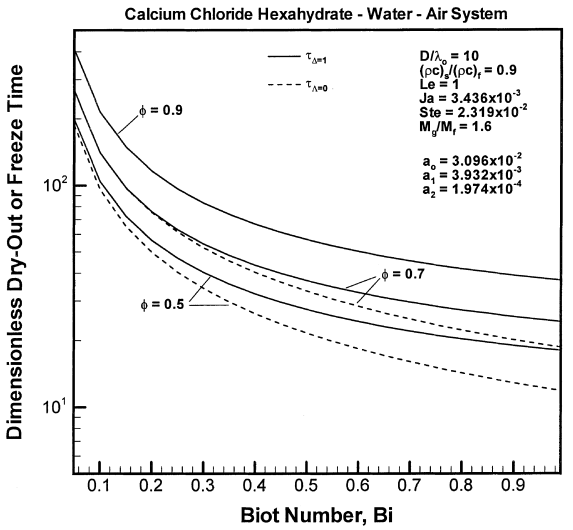

Fig. 9. Comparison of fluid layer evaporation time (dry-out) and material freeze time as a function of Biot number for selected relative humidities.

complete solidification is shown to occur between relative humidities of 84 and 86%, which corresponds to the intersection of the dry-out time curve ($\tau_{\Lambda=0}$) and the freeze time curve ($\tau_{\Delta=1}$). However, at $Bi = 10$, there is no transition and dry-out always occurs, independent of the relative humidity.

Fig. 9 shows the effect of Biot number (up to unity) on the dry-out time or freeze time for relative humidities of 50%, 70%, and 90%. As to be expected, increasing the Biot number decreases the dry-out or freeze time due to convective enhancement of heat transfer (and mass transfer due to the analogy between heat and mass transfer). In the figure, a transition is shown to occur at 70% relative humidity, with the transition Biot number bounded between 0.15 and 0.2. At 90% relative humidity, no transition occurs and complete solidification takes place throughout the entire Biot number range. On the other hand, at 50% relative humidity, no transition occurs and dry-out takes place for all representative Biot numbers.

6. Summary

A one-dimensional model of a solidifying slab subject to evaporative cooling at one of its surfaces was developed. A general semi-analytic solution was presented in the limit of low Stefan numbers and mass transfer rates. In developing the semi-analytic solution, an *n*th order polynomial was used to express the vapor pressure function in terms of fluid layer temperature. The freezing of a slab of calcium chloride hexahydrate subject to evaporative cooling of a thin layer of water into air was used to illustrate the utility of the model. A limiting case of isothermal cooling was used to compare the semi-analytic results to previously published results on the solidification of a slab subject to an isothermal boundary condition. Results showed the existence of a transition region, depending upon the relative humidity and Biot number, where fluid layer dry-out time competes with the solidification time of the slab.

References

[1] S. Ghosal, A. Emami-Naeini, Y.P. Harn, B.S. Draskovich, J.P. Pollinger, A physical model for the drying of gelcast ceramics, J. Am. Ceram. Soc. 82 (3) (1999) 513–520.
[2] S.K. Sastry, Factors affecting shrinkage of foods in refrigerated storage, ASHRAE Trans. 91 (1985) 683–689.
[3] J. Huang, L.S. Bartell, Electron diffraction studies of the kinetics of phase changes in clusters, J. Phys. Chem. 98 (17) (1994) 4543–4550.
[4] C.A. Hall, III, Evaporative cooling effects in precision machine tools, S.M. Thesis, Massachusetts Institute of Technology, Cambridge, MA, 1995.
[5] A. Bar-Cohen, Gas-assisted evaporative cooling of high density electronic modules, IEEE Trans. Components, Packaging and Manufact. Technol. – Part A 18 (1995) 502–509.
[6] G.N. Dulnev, V.A. Korablyev, A.V. Sharkov, Evaporation cooling of high power electronic devices, IEEE Trans. Components, Packaging and Manufact. Technol. – Part A 19 (1996) 431–434.
[7] W.M. Yan, T.F. Lin, Evaporative cooling of liquid film through interfacial heat and mass transfer in a vertical channel – II. Numerical study, Int. J. Heat Mass Transfer 34 (4–5) (1991) 1113–1124.
[8] S.S. Kachhwaha, P.L. Dhar, S.R. Kale, Experimental studies and numerical simulation of evaporative cooling of air with a water spray – I. Horizontal parallel flow, Int. J. Heat Mass Transfer 41 (2) (1998) 447–464.
[9] V. Alexiades and A.D. Solomon, Mathematical Modeling of Melting and Freezing Processes, 1st ed., Hemisphere, Washington, DC, 1993.
[10] J.S. Goodling, M.S. Khader, Inward solidification with radiation–convection boundary condition, ASME J. Heat Transfer 96 (1974) 114–115.
[11] B.T.F. Chung, L.T. Yeh, Solidification and melting of materials subject to convection and radiation, AIAA J. Spacecraft Rockets 12 (6) (1975) 329–333.
[12] M.M. Yan, P.N.S. Huang, Perturbation solutions to phase change problem subject to convection and radiation, ASME J. Heat Transfer 101 (1979) 96–100.
[13] R.V. Seeniraj, T.K. Bose, One-dimensional phase-change problems with radiation–convection, ASME J. Heat Transfer 104 (1982) 811–813.
[14] M. Prud'homme, T.H. Nguyen, D.L. Nguyen, A heat transfer analysis for solidification of slabs, cylinders and spheres, ASME J. Heat Transfer 111 (1989) 699–705.

[15] C.A. Hall, III, E.K. Glakpe, and J.N. Cannon, Unified semi-analytic solutions for freezing with two coalescing fronts, Int. Commun. Heat and Mass Transfer 26 (6) (1999) 751–759.
[16] J.H. Lienhard, A Heat Transfer Textbook, 2nd ed., Prentice-Hall, Englewood Cliffs, New Jersey, 1987, pp. 565, 576.
[17] W.M. Kays and M.E. Crawford, Convective Heat and Mass Transfer, 3rd ed., McGraw-Hill, New York, 1993, pp. 518–519.
[18] G.J. Van Wylen and R.E. Sonntag, Fundamentals of Classical Thermodynamics, 3rd ed., Wiley, New York, 1985, p. 635.